Geophysical Research Letters

RESEARCH LETTER
10.1029/2023GL104661

# Contrasting Trends and Drivers of Global Surface and Canopy Urban Heat Islands

**Huilin Du[1], Wenfeng Zhan[1,2], James Voogt[3], Benjamin Bechtel[4], T. C. Chakraborty[5], Zihan Liu[1], Leiqiu Hu[6], Zhihua Wang[7], Jiufeng Li[1], Peng Fu[8], Weilin Liao[9], Ming Luo[9], Long Li[1], Shasha Wang[1], Fan Huang[1], and Shiqi Miao[1]**

[1]Jiangsu Provincial Key Laboratory of Geographic Information Science and Technology, International Institute for Earth System Science, Nanjing University, Nanjing, China, [2]Jiangsu Center for Collaborative Innovation in Geographical Information Resource Development and Application, Nanjing, China, [3]Department of Geography, Western University, London, Ontario, Canada, [4]Department of Geography, Ruhr-University Bochum, Bochum, Germany, [5]Atmospheric Sciences and Global Change Division, Pacific Northwest National Laboratory, Richland, WA, USA, [6]Department of Atmospheric Science, University of Alabama in Huntsville, Huntsville, AL, USA, [7]School of Sustainable Engineering and the Built Environment, Arizona State University, Tempe, AZ, USA, [8]Center for Environment, Energy, and Economy, Harrisburg, PA, USA, [9]Guangdong Key Laboratory for Urbanization and Geo-simulation, School of Geography and Planning, Sun Yat-sen University, Guangzhou, China

**Key Points:**

- The global $I_s$ trend is six-fold and twofold larger than the $I_c$ trend during the day and at night, respectively
- During the day, global $I_s$ trend is slightly more controlled by surface property, yet background climate plays a dominant role in $I_c$ trend
- At night, both global $I_s$ and $I_c$ trends are more regulated by background climate

**Supporting Information:**

Supporting Information may be found in the online version of this article.

**Correspondence to:**

W. Zhan,
zhanwenfeng@nju.edu.cn

**Citation:**

Du, H., Zhan, W., Voogt, J., Bechtel, B., Chakraborty, T. C., Liu, Z., et al. (2023). Contrasting trends and drivers of global surface and canopy urban heat islands. *Geophysical Research Letters*, *50*, e2023GL104661. https://doi.org/10.1029/2023GL104661

Received 23 MAY 2023
Accepted 28 JUL 2023

**Abstract** A comprehensive comparison of the trends and drivers of global surface and canopy urban heat islands (termed $I_s$ and $I_c$ trends, respectively) is critical for better designing urban heat mitigation strategies. However, such a global comparison remains largely absent. Using spatially continuous land surface temperatures and surface air temperatures (2003–2020), here we find that the magnitude of the global mean $I_s$ trend (0.19 ± 0.006°C/decade, mean ± SE) for 5,643 cities worldwide is nearly six-times the corresponding $I_c$ trend (0.03 ± 0.002°C/decade) during the day, while the former (0.06 ± 0.004°C/decade) is double the latter (0.03 ± 0.002°C/decade) at night. Variable importance scores indicate that global daytime $I_s$ trend is slightly more controlled by surface property, while background climate plays a more dominant role in regulating global daytime $I_c$ trend. At night, both global $I_s$ and $I_c$ trends are mainly controlled by background climate.

**Plain Language Summary** Surface and canopy urban heat islands (surface and canopy UHIs, termed $I_s$ and $I_c$) are two major UHI types. These two counterparts are both related to urban population heat exposure and have long been a focus of urban climate research. However, the differences in the trends and major determinants of $I_s$ and $I_c$ over global cities remain largely unclear. Based on spatially continuous land surface temperature and surface air temperature observations from 2003 to 2020, we find that the global mean $I_s$ trends are about 6.3 times and 2 times the $I_c$ trends during the day and at night, respectively. During the day, the global $I_s$ trend is more regulated by surface property than by background climate, and vice versa for global $I_c$ trend. At night, both the global $I_s$ and $I_c$ trends are mainly regulated by background climate. These findings are important for better understanding global urban climate change and informing heat mitigation strategies.

## 1. Introduction

The urban heat island (UHI) can make urban lands warm up faster than the global average (Liu et al., 2022). The UHI and its trends hold important implications for eco-environments (Sarrat et al., 2006), climate change adaptation (Kleerekoper et al., 2012), energy consumption (Santamouris, 2014), and public health (Masselot et al., 2023), with urban heat-related deaths projected to surpass 0.1 million per year by 2050 (WHO, 2014). Accurate quantifications of UHI trends and associated drivers across global cities are critical steps toward understanding required urban heat mitigation and alleviating their potential negative effects.

There are generally two major UHI types (Oke et al., 2017), the surface UHI ($I_s$), defined as urban-rural contrast in land surface temperature (LST), and the canopy UHI ($I_c$), described as urban-rural contrast in surface air temperature (SAT). While the $I_s$ and $I_c$ differ conceptually and numerically, these two counterparts are well connected through urban land−atmosphere interactions (Venter et al., 2021). Satellite-based $I_s$ provides necessary and comprehensive LST estimates over both urban and rural surfaces (Peng et al., 2012), but these estimates are not sufficient to characterize heat stress within urban canopies, especially during daytime (Chakraborty et al., 2022). By contrast, the $I_c$ is generally more relevant to thermal comfort perceived by urban residents (Luo

& Lau, 2021). Thus, simultaneous investigations of global $I_s$ and $I_c$ trends are critical for better assessing global urban climate change and designing more appropriate urban heat mitigation strategies.

The ubiquitous nature of satellite LST observations has led to a recent explosion of examinations of $I_s$ trends even at the global scale (Chakraborty & Lee, 2019; Chen et al., 2021; Si et al., 2022; Yao et al., 2019). By comparison, the monitoring of $I_c$ trends often relies on SAT measurements from representative weather stations over urban and rural lands (Levermore et al., 2018; Li et al., 2018; Varquez & Kanda, 2018; Wang & Shu, 2020). However, traditional weather stations are often sparsely and unevenly distributed across cities worldwide (Rohde et al., 2013); recently emerging crowdsourced data can deliver high-density SAT measurements, but such data are unable to provide long-term measurements required for $I_c$ trend estimation (Meier et al., 2017). It is therefore not an easy task to obtain long-term and spatially dense urban and rural SAT measurements required for accurately estimating $I_c$ trends across an adequate number of cities worldwide. Despite such difficulties, few attempts have estimated the global $I_c$ trends by properly selecting available urban stations (Varquez & Kanda, 2018). However, these estimated $I_c$ trends may be highly sensitive to the site selection due to the high heterogeneity of urban surfaces; they may also be substantially influenced by the insufficient representation of global cities due to the uneven distribution of stations worldwide. Furthermore, their obtained global $I_c$ trends are not directly comparable to previously quantified global $I_s$ trends, mostly due to the discrepancies in study period, study area, and urban-rural delineations. To address these issues, a recent pioneering research compared the $I_s$ and $I_c$ trends over 200-plus megacities in mainland China based on spatially continuous SAT products estimated from satellite LST, in situ SAT, and other highly related variables (Yao et al., 2021). However, these estimated $I_s$ and $I_c$ trends may be overestimated due to the inclusion of newly urbanized surfaces in the urban delineation, because these newly urbanized surfaces possess very rapid warming trends when being converted from natural to urban lands during the study period (Liu et al., 2022; Luo & Lau, 2021). More importantly, it remains unknown whether these regional conclusions can be extended to broader climatic and geographic regions. Therefore, the differences in the relative magnitude of $I_s$ and $I_c$ trends across global cities remain largely vague.

The UHI trends are expected to be jointly regulated by surface properties (SFP; e.g., vegetation coverage), background climate (BGC; e.g., surface air temperature), and overall urban metrics (OUM, e.g., city size), together with their changes over time (Du et al., 2021; Oke et al., 2017; Peng et al., 2012; Venter et al., 2021). Nevertheless, the differences in the major determinants of $I_s$ and $I_c$ trends have not yet been investigated simultaneously even at regional scales. Case studies that separately investigated global $I_s$ or $I_c$ trends through statistical analyses have illustrated that the global $I_s$ trends are well correlated with the trends of urban-rural contrast in vegetation coverage during the daytime while related to those in surface albedo at night (Chakraborty & Lee, 2019; Si et al., 2022; Yao et al., 2019); and the global $I_c$ trends are correlated with vegetation coverage and wind speed, among other factors (Varquez & Kanda, 2018). However, the conclusions of these two types of studies cannot be directly compared due to their different study criteria. Besides, the chosen variables used for previous attribution analysis are relatively limited, and the associated methods (e.g., linear correlation analysis) may be insufficient to characterize the contrasting drivers between global $I_s$ and $I_c$ trends. Therefore, a comprehensive comparison of the drivers between global $I_s$ and $I_c$ trends, especially using the same sample and uniform criteria, remains lacking.

To address these gaps, here we compare the $I_s$ and $I_c$ trends across 5,643 cities worldwide spanning diverse climatic and geographical contexts, using spatially continuous MODIS LST observations and SAT estimates (2003–2020). We further choose 16 variables including BGC, SFP, and OUM factors, and compare their contributions to global $I_s$ and $I_c$ trends using random forest (RF) models. We believe this study can deepen our understanding of urban thermal environmental dynamics in the context of rapid urbanization and global climate change.

## 2. Material and Methods

### 2.1. Study Area and Data

We chose 5,643 cities worldwide (each with the urban area >10 $km^2$ in the year 2000) for this study (Figure S1 and Text S1 in Supporting Information S1). We employed the MODIS data, SAT data, reanalysis data, and auxiliary data from 2003 to 2020 to assist analysis (Table S1 in Supporting Information S1). The 8-day LST data (MYD11A2; 1 km) were used to calculate the $I_s$ trend. Here we used the Aqua-based LST mainly because the Aqua overpass times are relatively close to those of the daily maximum and minimum SATs (Oke et al., 2017). The 16-day enhanced vegetation index (EVI; MOD13A2; 1 km), 16-day white sky albedo (WSA; MCD43A3;

500 m), and daily aerosol optical depth (AOD; MCD19A2; 1 km) were employed to investigate the drivers of UHI trends. The yearly land cover type data (MCD12Q1; 500 m) were used to help delineate urban and rural surfaces. The daily maximum and minimum SAT data with a spatial resolution of 1 km were obtained from Zhang et al. (2022) and were used to calculate the $I_c$ trend. These SATs were estimated from LST observations, topography, and in situ measurements from >100,000 weather stations, and they have been shown to have higher accuracy compared to other global datasets. The monthly SAT, precipitation (PREP), and shortwave net radiation (RAD) from ERA5-Land reanalysis products (0.1°; Muñoz Sabater, 2019) were employed to investigate the impacts from BGC on UHI trends. The global urban boundary data from Li et al. (2020) were used for urban and rural delineation. The global impervious surface data (Global artificial impervious area (GAIA) data set; 30 m; Gong et al., 2020) were applied to examine the impacts of ISP on UHI trends. The population data (GPWv411 data set; 30 arc sec; Doxsey-Whitfield et al., 2015) were used to group global cities as well as to investigate their impacts on UHI trends. All satellite data were resampled to 1 km to match the spatial resolution of LST product.

### 2.2. Delineation of Urban and Rural Areas

Cities can experience significant urban expansion on decadal timescales (Liu et al., 2020). It is therefore necessary to control for changes in both urban and rural surfaces to allow a fair comparison of UHI intensities over years (Oke et al., 2017). To reduce the impacts from urban expansion on the calculation of UHI intensity trends, we defined urban surfaces as the pixels within the urban boundary in 2000, and delineated the rural surroundings as the ring areas between the 10-km and 100-km buffer zones outside the urban boundary in 2018 (Luo & Lau, 2018; Yao et al., 2019). The overlap of neighboring buffer zones was considered as rural surfaces for multiple urban areas (Yao et al., 2019). The pixels labeled as "water", "snow and ice", and "permanent wetlands" were further eliminated (Lai et al., 2018). Here we employed the urban boundary in 2018 to generate buffer zones mainly to characterize the rural background more accurately. We excluded surfaces within the 10 km buffer zone of urban area mainly because the inclusion of surfaces very close to the urban area may underestimate the UHI intensity (Zhou et al., 2015). A closer sensitivity analysis further demonstrated that both the patterns and magnitudes of global UHI trends rarely change with different buffer zone sizes (Figures S2 and S3 in Supporting Information S1).

### 2.3. Estimation and Comparison of Global $I_s$ and $I_c$ Trends

For $I_s$, we first disregarded the pixels with retrieval error larger than 3.0 K according to the quality-control band of MYD11A2 and then aggregated these observations into monthly composites to reduce the uncertainties arising from retrieval processes and cloud contaminations (Lai et al., 2018; Venter et al., 2021). For $I_c$, we first removed the SAT anomalies using $3\sigma$ rule for each pixel and similarly aggregated them into monthly composites. $I_s$ (or $I_c$) was estimated as the difference in the mean LST (or SAT) between all available urban and rural pixels (Du et al., 2021; Peng et al., 2012), and their long-term trends were then quantified by linearly regressing the variable against the year (Chakraborty & Lee, 2019; Varquez & Kanda, 2018). We compared the $I_s$ and $I_c$ trends across different continents, climate zones, and cities with different sizes. It is important to note that the quantification of $I_c$ trends may be impacted by the estimation error of SAT product. More discussions and cross-validations on this issue are provided in Text S2 in Supporting Information S1.

### 2.4. Comparison of the Drivers Between Global $I_s$ and $I_c$ Trends

The drivers of absolute $I_s$ and $I_c$ can be categorized into three groups, including the BGC factors (e.g., SAT and PREP), SFP factors (e.g., ISP and EVI), and OUM factors (e.g., city size) (Du et al., 2021; Peng et al., 2012; Venter et al., 2021). It is therefore expected that the long-term trends of $I_s$ and $I_c$ are also regulated by these factors, together with their changes over time. Here we selected the explanatory factors using two criteria: (a) the factor has been shown to be important for explaining UHI dynamics, and (b) the factor is consistent and easily obtainable across global cities. We chose SAT, PREP, ΔAOD (with the prefix "Δ" denoting the urban-rural contrast), and RAD as the BGC factors, ΔISP, ΔEVI, and ΔWSA as the SFP factors, and urban area (Area) and urban population (POP) as the OUM factors. Note that the multicollinearity among variables can distort the estimation of the relative importance of factors (Venter et al., 2021). We therefore only reserved the variables with variance inflation factor <5.0 (Zuur et al., 2010), including eight variables (i.e., Area, SAT, PREP, ΔAOD,

RAD, ΔISP, ΔEVI, and ΔWSA; calculated as the mean value during the study period) together with their trends (i.e., $K_{Area}$, $K_{SAT}$, $K_{PREP}$, $K_{\Delta AOD}$, $K_{RAD}$, $K_{\Delta ISP}$, $K_{\Delta EVI}$, and $K_{\Delta WSA}$). Referring to previous studies (Seto et al., 2011), the $K_{Area}$ was calculated as $100 \times ((Area_{end}/Area_{start})^{1/n} - 1)$ to more accurately characterize urban expansion processes, where $Area_{end}$ and $Area_{start}$ denote the urban area of the start year and end year, respectively, and $n$ represents the length of study period.

We employed partial correlation analysis and RF model to compare the drivers of $I_s$ and $I_c$ trends. The partial correlation coefficient was used to determine the positive or negative relationships between UHI trends and a certain factor while holding the other factors constant. The RF model was employed for measuring the variable importance (unit: %) of the chosen factors to $I_s$ and $I_c$ trends. The overall relative importance of a certain category was calculated as the addition of all its subcategory variables, for example, the relative importance of OUM was estimated as the addition of those of Area and $K_{Area}$. This study employed 80% of the samples as training data and the rest were used for validation. The performance of RF models was evaluated using the coefficient of determination ($R^2$). The comparison of the drivers between global $I_s$ and $I_c$ trends was performed at both annual and seasonal scales.

## 3. Results and Discussion

### 3.1. Contrasting Trends Between $I_s$ and $I_c$

In general, the global $I_s$ trend (0.19 ± 0.006°C/decade, mean ± SE, $p < 0.05$) is nearly six times larger than the $I_c$ trend (0.03 ± 0.002°C/decade, $p < 0.05$) during the day, with 70% and 67% of cities showing increasing trends in $I_s$ and $I_c$, respectively (Figures 1a–1c). At night, the $I_s$ and $I_c$ trends are much closer, with the former (0.06 ± 0.004°C/decade, $p < 0.05$) twice the magnitude of the latter (0.03 ± 0.002°C/decade, $p < 0.05$). The proportions of cities exhibiting warming trends in nocturnal $I_s$ and $I_c$ are 58% and 59%, respectively (Figure 1d–1f). These results imply a notable increasing trend in LST-based diurnal temperature range change ($\Delta DTR_{LST}$, i.e., equivalent to daytime minus nighttime $I_s$ of 0.13°C/decade, $p < 0.05$) yet an insignificant trend in SAT-based diurnal temperature range change ($\Delta DTR_{SAT}$, equivalent to daytime minus nighttime $I_c$ of about 0.00°C/decade, $p > 0.05$) in recent decades (Figure S4 in Supporting Information S1). In terms of the urban–rural contrast in warming rate (Figure S5 and Table S2 in Supporting Information S1), the global urban warming rate estimated from LST observations (0.53°C/decade; averaged for daytime and nighttime) is 1.3 times that of the rural surroundings (0.40°C/decade), while such a ratio is reduced to 1.1 (urban and rural warming rates are 0.39°C/decade and 0.36°C/decade, respectively) when using SAT measurements.

Both the $I_s$ and $I_c$ trends exhibit notable spatial variations (Figures 1g–1n). For Asian cities, the daytime $I_s$ and $I_c$ trends are 0.31°C/decade and 0.07°C/decade, respectively, and the corresponding nighttime trends are 0.17°C/decade and 0.09°C/decade, respectively (Figure S6 in Supporting Information S1). By contrast, for European cities with more stable urban land, both the $I_s$ and $I_c$ trends are less pronounced during the day (0.07°C/decade for $I_s$ and −0.01°C/decade for $I_c$) and even negative at night (−0.03°C/decade for $I_s$ and −0.01°C/decade for $I_c$; Figure S6 in Supporting Information S1). Both the slightly larger urban densification trends (identified by $K_{ISP}$) and the substantially faster rural than urban greening (identified by $K_{EVI}$) in Asian cities compared to European cities may contribute to the disparities in UHI trends between these two continents (Figure S7 in Supporting Information S1). Further illustrations on the impacts of $K_{ISP}$ and $K_{EVI}$ on the $I_s$ and $I_c$ trends are provided in Section 3.2.

From a climatic perspective, during the day, the $I_s$ trend reaches its maximum in equatorial climates (0.30°C/decade), followed by temperate (0.27°C/decade) and snow climates (0.16°C/decade), while the $I_s$ exhibits a decreasing trend for arid climates (−0.03°C/decade; Figure 2c), which are in relatively good agreements with previous results (Si et al., 2022). By comparison, the $I_c$ trends show diametrically opposite climatic patterns to those of $I_s$, that is, the maximum $I_c$ trend occurs in snow climates (0.034°C/decade), followed by temperate (0.030°C/decade), arid (0.028°C/decade), and equatorial (0.007°C/decade) climates (Figure 2c). At night, the $I_s$ and $I_c$ trends show very similar climatic variations, with larger values in equatorial and arid climates than in temperate and snow climates (Figure 2d).

Interestingly, we find that the $I_s$ and $I_c$ trends generally increase with urban population (Figures 2e and 2f), and there are significant positive relationships between both $I_s$ and $I_c$ trends and the logarithm of urban population (Figure S8 in Supporting Information S1). During the day, both the $I_s$ and $I_c$ trends of POP-1 cities are notably lower than those of POP-2, POP-3 and POP-4 cities (Figure 2e). At night, the $I_s$ trend increases continuously with

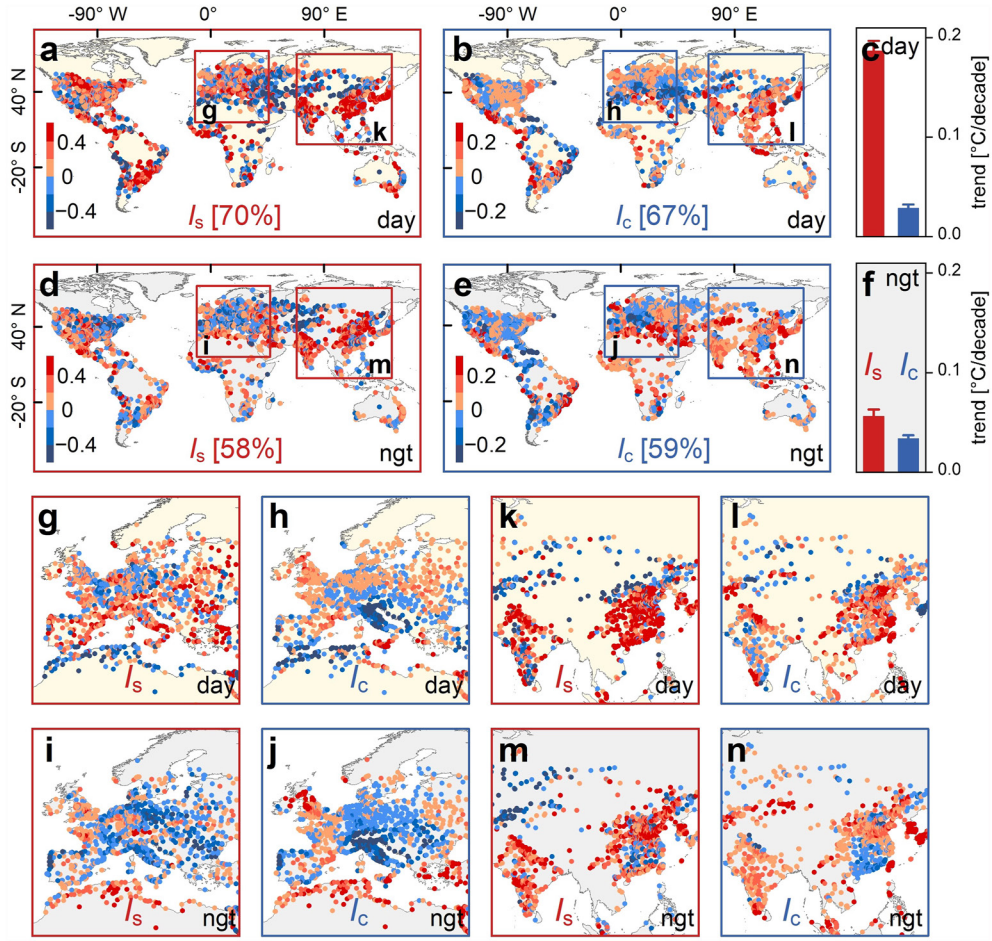


**Figure 1.** The annual mean $I_s$ and $I_c$ trends across 5,643 cities worldwide over 2003−2020 | The $I_s$ trends during the day (a) and night (d), the $I_c$ trends during the day (b) and night (e), and the global mean $I_s$ and $I_c$ trends for the day (c) and night (f). The percentages in brackets indicate the proportion of cities with positive UHI intensity trends. Panel (g) to (n) show the enlarged rectangular regions within (a), (b), (d) and (e), with their red and blue boxes indicating the $I_s$ and $I_c$ trends, respectively. The error bars in (c) and (f) denote the 99% confidence interval.

population size, while the $I_c$ trend is characterized by an initial decrease from POP-1 to POP-2 cities and then a steady increase from POP-2 to POP-4 cities (Figure 2f). With respect to seasonal variations, both the daytime $I_s$ and $I_c$ trends are characterized by a notably higher trend in summer (0.36°C/decade for $I_s$ and 0.07°C/decade for $I_c$) than in other seasons (Figures 2g and 2h). At night, the seasonal pattern of the $I_s$ trends holds a similar fashion to that of daytime, while the $I_c$ trends become larger in spring and summer than in autumn and winter.

### 3.2. Contrasting Drivers Between $I_s$ and $I_c$ Trends

The results reveal that the $R^2$ of RF models are 0.50 and 0.44 for global daytime and nighttime $I_s$ trends, respectively, and are 0.44 and 0.48 for global daytime and nighttime $I_c$ trends, respectively. During the day, the global $I_s$ trend is slightly more controlled by SFP than by BGC (Figure 3a), with the impacts from SFP reaching the maximum (64%) and minimum (45%) in summer and winter, respectively (Figure S9 in Supporting Information S1). By comparison, BGC plays a more dominant role in regulating global $I_c$ trend relative to SFP (Figure 3a), and the BGC impacts are more pronounced in autumn (68%), followed by summer (61%), winter (57%), and spring (56%) (Figure S9 in Supporting Information S1). At night, both the global $I_s$ and $I_c$ trends are more controlled by BGC than by SFP (Figure 3a), with the impacts from BGC much lower in winter than in other seasons for both $I_s$ and $I_c$ trends (Figure S9 in Supporting Information S1). From a climatic perspective (Figure 3b−3e), the relative importance among different categories of drivers in equatorial and temperate climates follows a similar pattern

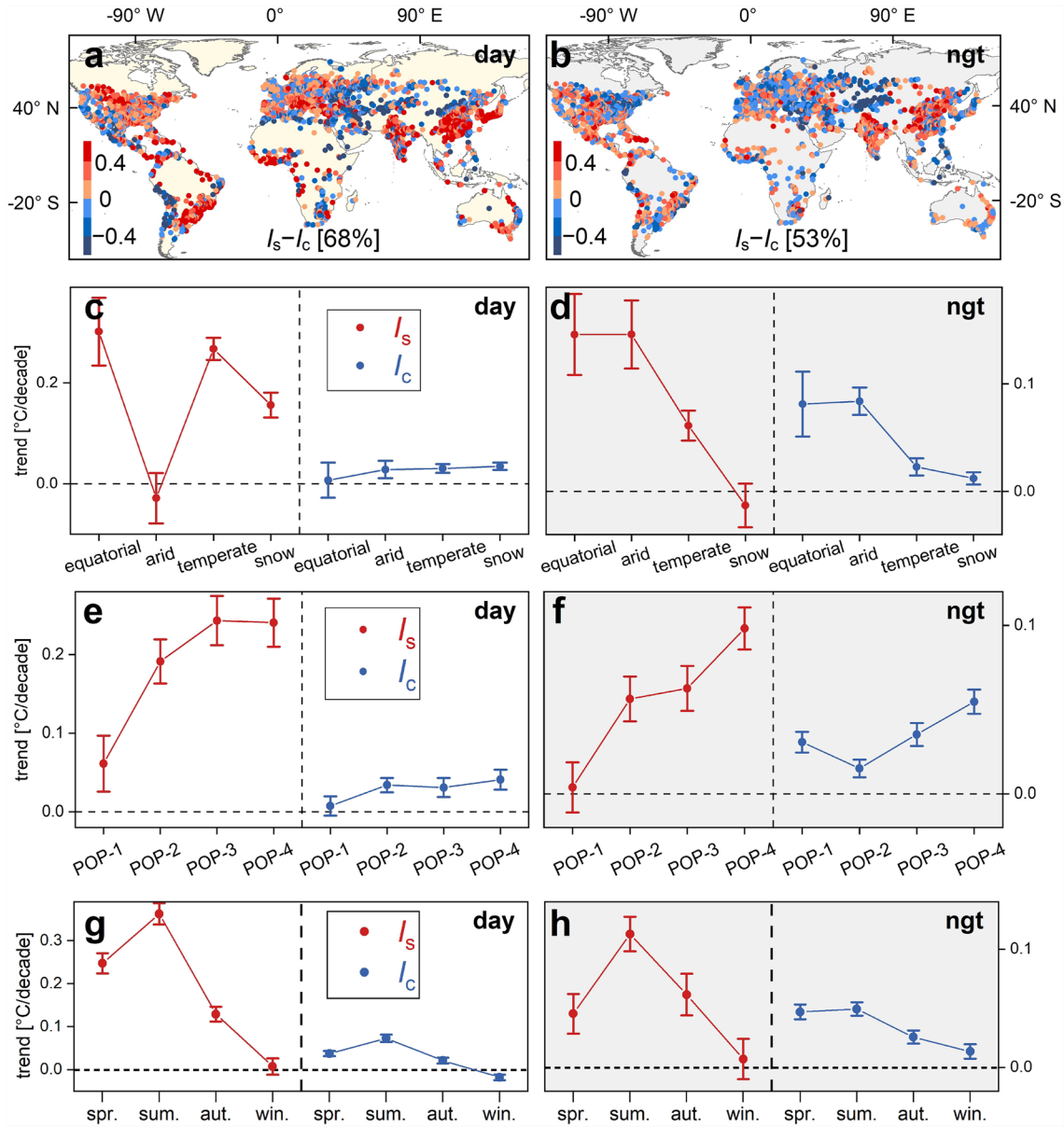


**Figure 2.** The differences between the annual mean $I_s$ and $I_c$ trends (i.e., $I_s - I_c$) across global cities as well as comparisons of $I_s$ and $I_c$ trends in different climate zones, city sizes, and seasons | The patterns of $I_s - I_c$ trend for the day (a) and night (b), with the percentages in brackets indicating the proportion of cities with a larger trend of $I_s$ than of $I_c$; the $I_s$ and $I_c$ trends across different climate zones, city sizes (denoted by urban population, with "POP-1" to "POP-4" representing the ascending order of urban population, refer to Text S1 in Supporting Information S1), and seasons for the day (c, e, and g) and night (d, f, and h). The error bars in (c–h) denote the 99% confidence interval.

to that over the globe (Figures 3b and 3d). For cities in arid climates, SFP serves as the dominant regulator of the $I_s$ trend, while the $I_c$ trend is more regulated by BGC during both daytime and nighttime (Figure 3c). For cities in snow climates, both the $I_s$ and $I_c$ trends are significantly more controlled by BGC relative to SFP (Figure 3e).

The relative importance of regulators on the UHI intensity trends depends on the UHI type (i.e., $I_s$ or $I_c$) and time of day (Figure 3a). Across global cities, the daytime $I_s$ trend is mostly regulated by $K_{\Delta EVI}$ (reaching 25%) among all the regulators, which is on par with the magnitude reported previously (Chen et al., 2021; Yao et al., 2019). This is understandable because Earth's surface has been increasingly greening over the past two decades due to $CO_2$ fertilization, nitrogen deposition, and climate change (Chen et al., 2019; Zhu et al., 2016), which greatly enhances the evapotranspiration efficiency of rural surfaces and thus increases global daytime $I_s$ (Figures S10 and S11a in Supporting Information S1). For the global daytime $I_c$ trend, PREP (13%) and ΔAOD (11%) contribute

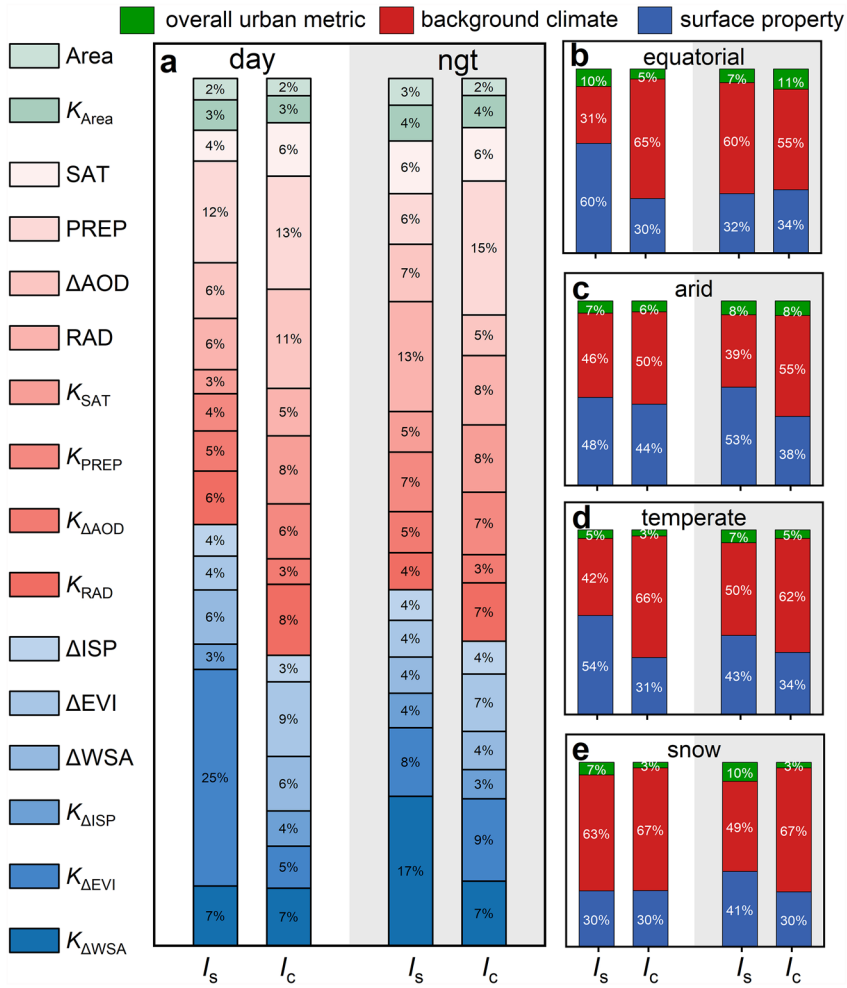


**Figure 3.** Relative importance of different types of controls to annual mean $I_s$ and $I_c$ trends for all the cities (a), cities in equatorial (b), arid (c), temperate (d), and snow climates (e) | Three types of controls are involved. City area (Area) and its trend ($K_{Area}$) belong to the overall urban metric (OUM) category; surface air temperature (SAT), precipitation (PREP), urban-rural contrast in aerosol optical depth (ΔAOD), shortwave net radiation (RAD), and their associated trends ($K_{SAT}$, $K_{PREP}$, $K_{ΔAOD}$, and $K_{RAD}$) belong to the background climate (BGC) category; and urban-rural contrast in impervious surface percentage (ΔISP), enhanced vegetation index (ΔEVI), white sky albedo (ΔWSA), and their trends ($K_{ΔISP}$, $K_{ΔEVI}$, and $K_{ΔWSA}$) belong to the surface property (SFP) category.

slightly more than the other regulators. At night, $K_{ΔWSA}$ serves as the largest regulator (17%) to the global $I_s$ trend, and a smaller $K_{ΔWSA}$ is usually accompanied by a larger nighttime $I_s$ trend (Figures S10 and S11b in Supporting Information S1). In comparison, the nighttime $I_c$ trend is more controlled by PREP (15%) than by the other regulators.

## 4. Clarifications and Implications

Simultaneous investigation of $I_s$ and $I_c$ has long been of interest to the urban climate community. The contrasting patterns and drivers between global $I_s$ and $I_c$ at the intra-annual timescale have been well understood (Du et al., 2021). However, the differences between these two variables remain poorly understood from an interdecadal perspective, mainly due to the difficulty of obtaining long-term and spatially dense SAT measurements within global cities. By combining spatially continuous MODIS LST observations and SAT estimates (Zhang et al., 2022), here we provide a first global evaluation of the $I_c$ trends and demonstrate that these trends are only one-sixth and one-half of those based on LSTs during daytime and nighttime, respectively (Figure 1). From the urban warming perspective, we reconfirm the findings of a very recent literature that LST-based

global urban to rural warming rate ratio is 1.3 (Liu et al., 2022), while we, for the first time to the best of knowledge, provide evidence that such a ratio is reduced to 1.1 when using SAT measurements that hold more important implications for public health considerations (Figure S5 in Supporting Information S1). These results suggest the caution of incorporating LST or SUHI in epidemiological researches, which may significantly overestimate the trends of heat stress perceived by urban residents, especially once the local drying effects of urbanization is also taken into consideration (Chakraborty et al., 2022). From the urban climatology perspective, the contrasting patterns of the $I_s$ and $I_c$ trends revealed by this study also better clarify the temporal evolution of urban surface-atmosphere interaction in the recent two decades (Oke et al., 2017), which may help improve the accuracy of global urban climate models. Besides, we show that these $I_s$ and $I_c$ trends are prone to be higher in more populous cities (Figures 2e–2f; Figure S8 in Supporting Information S1). This implies an augmented urban population exposure to urban warmth and a greater urgency of urban heat mitigation in these populous cities, especially for tropical and subtropical cities that are already hot (Figures 2c–2d; Manoli et al., 2019).

Our attribution analysis reveals that $K_{\Delta EVI}$ and $K_{\Delta WSA}$ are the largest regulators of global daytime and nighttime $I_s$ trends, respectively, while global $I_c$ trends are more regulated by PREP during both daytime and nighttime (Figure 3a and Figure S11 in Supporting Information S1). These results suggest that increasing urban green infrastructure and surface albedo may serve as effective strategies to curb $I_s$ trends, yet they become less helpful in mitigating the $I_c$ trends, even though the $I_c$ serves as a more meaningful measure of increased thermal discomfort perceived by urban residents (compared with a rural reference; Stewart et al., 2021). Practitioners should therefore keep in mind that the benefits of these commonly used adaptation strategies to mitigate urban heat stress does not necessarily equal to those to alleviate the $I_s$ trends and that the design of urban heat mitigation strategies should not rely merely on $I_s$.

There may exist some limitations of this study. First, the quantified $I_s$ and $I_c$ trends have been demonstrated to be robust and reliable at global or regional scales (Text S2 in Supporting Information S1), while these trends may be less convincing in individual cities due to the potential uncertainties related to LSTs (e.g., thermal anisotropy, missing records due to cloud contamination) and SATs (e.g., weather stations used to estimate SATs are unevenly distributed within cities worldwide) (Chakraborty, Lee, et al., 2021; Du et al., 2023; Zhang et al., 2022). Second, like a couple of recent studies regarding the absolute UHI (Chakraborty, Sarangi, & Lee, 2021; Venter et al., 2021), this study investigates the drivers of $I_s$ and $I_c$ trends with RF models. These statistical approaches are not capable of disentangling the physical mechanism of UHI trends from the surface energy balance perspective, yet they still serve as an important complement to the physical attribution frameworks (Manoli et al., 2019; Zhang et al., 2023; Zhao et al., 2014). Future efforts are still needed to use multiple lines of evidence, including data- and process-based models, to understand these complex physical mechanisms.

## Conflict of Interest

The authors declare no conflicts of interest relevant to this study.

## Data Availability Statement

The 8-day land surface temperature (LST) data from MYD11A2 product are publicly available at https://e4ftl01.cr.usgs.gov/MOLA/MYD11A2.006/. The 16-day enhanced vegetation index (EVI) data from MOD13Q1 product are publicly available at https://e4ftl01.cr.usgs.gov/MOLT/MOD13Q1.006/. The 16-day white sky albedo (WSA) data from MCD43A3 are publicly available at https://e4ftl01.cr.usgs.gov/MOTA/MCD43A3.006/. The daily aerosol optical depth (AOD) from MCD19A2 are publicly available at https://e4ftl01.cr.usgs.gov/MOTA/MCD19A2.006/. The yearly land cover type data from MCD12Q1 can be found at https://e4ftl01.cr.usgs.gov/MOTA/MCD12Q1.006/. The daily maximum and minimum SAT products can be found here: https://iastate.figshare.com/browse. The reanalysis data (including SAT, precipitation, and radiation) from ERA5-Land products are publicly available at https://cds.climate.copernicus.eu/cdsapp#!/dataset/reanalysis-era5-land-monthly-means?tab=form. The global urban boundary (GUB) data set is accessible at http://data.starcloud.pcl.ac.cn/zh/resource/14. The Global artificial impervious area (GAIA) data are publicly available at http://data.starcloud.pcl.ac.cn/zh/resource/13. The population data from GPWv411 data set are available at https://sedac.ciesin.columbia.edu/data/set/gpw-v4-population-count-rev11/data-download.

**Acknowledgments**
We gratefully acknowledge the National Natural Science Foundation of China (42171306, 42001270, 42201337, and 41871029) for providing support for this current study. We also thank the support from the National Youth Talent Support Program of China. TC Chakraborty's contribution was supported by COMPASS-GLM, a multi-institutional project supported by the U.S. Department of Energy, Office of Science, Office of Biological and Environmental Research as part of the Earth and Environmental Systems Modeling program. Pacific Northwest National Laboratory is operated for the Department of Energy by Battelle Memorial Institute under contract DE-AC05-76RL01830.

## References

Chakraborty, T. C., & Lee, X. H. (2019). A simplified urban-extent algorithm to characterize surface urban heat islands on a global scale and examine vegetation control on their spatiotemporal variability. *International Journal of Applied Earth Observation and Geoinformation*, *74*, 269–280. https://doi.org/10.1016/j.jag.2018.09.015

Chakraborty, T. C., Lee, X. H., Ermida, S., & Zhan, W. F. (2021). On the land emissivity assumption and Landsat-derived surface urban heat islands: A global analysis. *Remote Sensing of Environment*, *265*, 112682. https://doi.org/10.1016/j.rse.2021.112682

Chakraborty, T. C., Sarangi, C., & Lee, X. H. (2021). Reduction in human activity can enhance the urban heat island: Insights from the COVID-19 lockdown. *Environmental Research Letters*, *16*(5), 054060. https://doi.org/10.1088/1748-9326/abef8e

Chakraborty, T. C., Venter, Z. S., Qian, Y., & Lee, X. H. (2022). Lower urban humidity moderates outdoor heat stress. *AGU Advances*, *3*(5), e2022AV000729. https://doi.org/10.1029/2022av000729

Chen, C., Li, D., & Keenan, T. F. (2021). Enhanced surface urban heat islands due to divergent urban-rural greening trends. *Environmental Research Letters*, *16*(12), 124071. https://doi.org/10.1088/1748-9326/ac36f8

Chen, C., Park, T., Wang, X. H., Piao, S. L., Xu, B. D., Chaturvedi, R. K., et al. (2019). China and India lead in greening of the world through land-use management. *Nature Sustainability*, *2*, 122–129. https://doi.org/10.1038/s41893-019-0220-7

Doxsey-Whitfield, E., MacManus, K., Adamo, S. B., Pistolesi, L., Squires, J., Borkovska, O., & Baptista, S. R. (2015). Taking advantage of the improved availability of census data: A first look at the gridded population of the world, version 4. *Applied Geography*, *1*(3), 226–234. https://doi.org/10.1080/23754931.2015.1014272

Du, H. L., Zhan, W. F., Liu, Z. H., Krayenhoff, E. S., Chakraborty, T. C., Zhao, L., et al. (2023). Global mapping of urban thermal anisotropy reveals substantial potential biases for remotely sensed urban climates. *Science Bulletin*. https://doi.org/10.1016/j.scib.2023.06.032

Du, H. L., Zhan, W. F., Liu, Z. H., Li, J. F., Li, L., Lai, J. M., et al. (2021). Simultaneous investigation of surface and canopy urban heat islands over global cities. *ISPRS Journal of Photogrammetry and Remote Sensing*, *181*, 67–83. https://doi.org/10.1016/j.isprsjprs.2021.09.003

Gong, P., Li, X. C., Wang, J., Bai, Y. Q., Chen, B., Hu, T. Y., et al. (2020). Annual maps of global artificial impervious area (GAIA) between 1985 and 2018. *Remote Sensing of Environment*, *236*, 111510. https://doi.org/10.1016/j.rse.2019.111510

Kleerekoper, L., Van Esch, M., & Salcedo, T. B. (2012). How to make a city climate-proof, addressing the urban heat island effect. *Resources, Conservation and Recycling*, *64*, 30–38. https://doi.org/10.1016/j.resconrec.2011.06.004

Lai, J. M., Zhan, W. F., Huang, F., Voogt, J., Bechtel, B., Allen, M., et al. (2018). Identification of typical diurnal patterns for clear-sky climatology of surface urban heat islands. *Remote Sensing of Environment*, *217*, 203–220. https://doi.org/10.1016/j.rse.2018.08.021

Levermore, G., Parkinson, J., Lee, K., Laycock, P., & Lindley, S. (2018). The increasing trend of the urban heat island intensity. *Urban Climate*, *24*, 360–368. https://doi.org/10.1016/j.uclim.2017.02.004

Li, G. D., Zhang, X., Mirzaei, P. A., Zhang, J. H., & Zhao, Z. S. (2018). Urban heat island effect of a typical valley city in China: Responds to the global warming and rapid urbanization. *Sustainable Cities and Society*, *38*, 736–745. https://doi.org/10.1016/j.scs.2018.01.033

Li, X. C., Gong, P., Zhou, Y. Y., Wang, J., Bai, Y. Q., Chen, B., et al. (2020). Mapping global urban boundaries from the global artificial impervious area (GAIA) data. *Environmental Research Letters*, *15*(9), 094044. https://doi.org/10.1088/1748-9326/ab9be3

Liu, X. P., Huang, Y. H., Xu, X. C., Li, X. C., Li, X., Ciais, P., et al. (2020). High-spatiotemporal-resolution mapping of global urban change from 1985 to 2015. *Nature Sustainability*, *3*(7), 564–570. https://doi.org/10.1038/s41893-020-0521-x

Liu, Z. H., Zhan, W. F., Bechtel, B., Voogt, J., Lai, J. M., Chakraborty, T. C., et al. (2022). Surface warming in global cities is substantially more rapid than in rural background areas. *Communications Earth & Environment*, *3*(1), 219. https://doi.org/10.1038/s43247-022-00539-x

Luo, M., & Lau, N. C. (2018). Increasing heat stress in urban areas of eastern China: Acceleration by urbanization. *Geophysical Research Letters*, *45*(23), 13060–13069. https://doi.org/10.1029/2018gl080306

Luo, M., & Lau, N. C. (2021). Increasing human-perceived heat stress risks exacerbated by urbanization in China: A comparative study based on multiple metrics. *Earth's Future*, *9*(7), e2020EF001848. https://doi.org/10.1029/2020ef001848

Manoli, G., Fatichi, S., Schläpfer, M., Yu, K. L., Crowther, T. W., Meili, N., et al. (2019). Magnitude of urban heat islands largely explained by climate and population. *Nature*, *573*(7772), 55–60. https://doi.org/10.1038/s41586-019-1512-9

Masselot, P., Mistry, M., Vanoli, J., Schneider, R., Iungman, T., Garcia-Leon, D., et al. (2023). Excess mortality attributed to heat and cold: A health impact assessment study in 854 cities in Europe. *The Lancet Planetary Health*, *7*(4), e271–e281. https://doi.org/10.1016/s2542-5196(23)00023-2

Meier, F., Fenner, D., Grassmann, T., Otto, M., & Scherer, D. (2017). Crowdsourcing air temperature from citizen weather stations for urban climate research. *Urban Climate*, *19*, 170–191. https://doi.org/10.1016/j.uclim.2017.01.006

Muñoz Sabater, J. (2019). ERA5-Land monthly averaged data from 1981 to present. *Copernicus Climate Change Service Climate Data Store*, *146*, 1999–2049.

Oke, T. R., Mills, G., Christen, A., & Voogt, J. A. (2017). *Urban climates*. Cambridge University Press.

Peng, S. S., Piao, S. L., Ciais, P., Friedlingstein, P., Ottle, C., Breon, F. M., et al. (2012). Surface urban heat island across 419 global big cities. *Environmental Science & Technology*, *46*(2), 696–703. https://doi.org/10.1021/es2030438

Rohde, R., Muller, R., Jacobsen, R., Perlmutter, S., Rosenfeld, A., Wurtele, J., et al. (2013). Berkeley earth temperature averaging process. *Geoinformatics Geostatistics an Overview*, *1*(02), 1–13. https://doi.org/10.4172/2327-4581.1000103

Santamouris, M. (2014). On the energy impact of urban heat island and global warming on buildings. *Energy and Buildings*, *82*, 100–113. https://doi.org/10.1016/j.enbuild.2014.07.022

Sarrat, C., Lemonsu, A., Masson, V., & Guedalia, D. (2006). Impact of urban heat island on regional atmospheric pollution. *Atmospheric Environment*, *40*(10), 1743–1758. https://doi.org/10.1016/j.atmosenv.2005.11.037

Seto, K. C., Fragkias, M., Güneralp, B., & Reilly, M. K. (2011). A meta-analysis of global urban land expansion. *PLoS One*, *6*(8), e23777. https://doi.org/10.1371/journal.pone.0023777

Si, M. L., Li, Z. L., Nerry, F., Tang, B. H., Leng, P., Wu, H., et al. (2022). Spatiotemporal pattern and long-term trend of global surface urban heat islands characterized by dynamic urban-extent method and MODIS data. *ISPRS Journal of Photogrammetry and Remote Sensing*, *183*, 321–335. https://doi.org/10.1016/j.isprsjprs.2021.11.017

Stewart, I. D., Krayenhoff, E. S., Voogt, J. A., Lachapelle, J. A., Allen, M. A., & Broadbent, A. M. (2021). Time evolution of the surface urban heat island. *Earth's Future*, *9*(10), e2021EF002178. https://doi.org/10.1029/2021ef002178

Varquez, A. C. G., & Kanda, M. (2018). Global urban climatology: A meta-analysis of air temperature trends (1960–2009). *Npj Climate and Atmospheric Science*, *1*, 32. https://doi.org/10.1038/s41612-018-0042-8

Venter, Z. S., Chakraborty, T. C., & Lee, X. H. (2021). Crowdsourced air temperatures contrast satellite measures of the urban heat island and its mechanisms. *Science Advances*, *7*(22), eabb9569. https://doi.org/10.1126/sciadv.abb9569

Wang, W., & Shu, J. (2020). Urban renewal can mitigate urban heat islands. *Geophysical Research Letters*, *47*(6), e2019GL085948. https://doi.org/10.1029/2019gl085948

World Health Organization. (2014). *Quantitative risk assessment of the effects of climate change on selected causes of death, 2030s and 2050s*. World Health Organization. Retrieved from https://apps.who.int/iris/handle/10665/134014

Yao, R., Wang, L. C., Huang, X., Gong, W., & Xia, X. G. (2019). Greening in rural areas increases the surface urban heat island intensity. *Geophysical Research Letters*, *46*(4), 2204–2212. https://doi.org/10.1029/2018gl081816

Yao, R., Wang, L. C., Huang, X., Liu, Y. T., Niu, Z. G., Wang, S. Q., et al. (2021). Long-term trends of surface and canopy layer urban heat island intensity in 272 cities in the mainland of China. *Science of the Total Environment*, *772*, 145607. https://doi.org/10.1016/j.scitotenv.2021.145607

Zhang, K. E., Cao, C., Chu, H. R., Zhao, L., Zhao, J. Y., & Lee, X. H. (2023). Increased heat risk in wet climate induced by urban humid heat. *Nature*, *617*(7962), 1–5. https://doi.org/10.1038/s41586-023-05911-1

Zhang, T., Zhou, Y. Y., Zhao, K. G., Zhu, Z. Y., Chen, G., Hu, J., & Wang, L. (2022). A global dataset of daily maximum and minimum near-surface air temperature at 1 km resolution over land (2003–2020). *Earth System Science Data*, *14*(12), 5637–5649. https://doi.org/10.5194/essd-14-5637-2022

Zhao, L., Lee, X. H., Smith, R. B., & Oleson, K. (2014). Strong contributions of local background climate to urban heat islands. *Nature*, *511*(7508), 216–219. https://doi.org/10.1038/nature13462

Zhou, D. C., Zhao, S. Q., Zhang, L. X., Sun, G., & Liu, Y. Q. (2015). The footprint of urban heat island effect in China. *Scientific Reports*, *5*, 1–11. https://doi.org/10.1038/srep11160

Zhu, Z. C., Piao, S. L., Myneni, R. B., Huang, M. T., Zeng, Z. Z., Canadell, J. G., et al. (2016). Greening of the Earth and its drivers. *Nature Climate Change*, *6*(8), 791–795. https://doi.org/10.1038/nclimate3004

Zuur, A. F., Ieno, E. N., & Elphick, C. S. (2010). A protocol for data exploration to avoid common statistical problems. *Methods in Ecology and Evolution*, *1*, 3–14. https://doi.org/10.1111/j.2041-210x.2009.00001.x

## References From the Supporting Information

Cao, L. J., Zhu, Y. N., Tang, G. L., Yuan, F., & Yan, Z. W. (2016). Climatic warming in China according to a homogenized data set from 2419 stations. *International Journal of Climatology*, *36*(13), 4384–4392. https://doi.org/10.1002/joc.4639

Didan, K. (2015). MOD13A2 MODIS/Terra vegetation indices 16-Day L3 Global 1km SIN Grid V006 [Dataset]. NASA EOSDIS Land Processes DAAC. Retrieved from https://ladsweb.modaps.eosdis.nasa.gov/missions-and-measurements/products/MOD13A2

Friedl, M., & Sulla-Menashe, D. (2019). MCD12Q1 MODIS/Terra+Aqua land cover type yearly L3 global 500m SIN grid V006 [Dataset]. NASA EOSDIS Land Processes DAAC. Retrieved from https://lpdaac.usgs.gov/products/mcd12q1v006/

Kottek, M., Grieser, J., Beck, C., Rudolf, B., & Rubel, F. (2006). World map of the Köppen-Geiger climate classification updated. *Meteorologische Zeitschrift*, *15*(3), 259–263. https://doi.org/10.1127/0941-2948/2006/0130

Lyapustin, A., & Wang, Y. (2018). MCD19A2 MODIS/Terra+Aqua land aerosol optical depth daily L2G global 1km SIN grid V006 [Dataset]. NASA EOSDIS Land Processes DAAC. Retrieved from https://lpdaac.usgs.gov/products/mcd19a2v006/

Ma, J., Zhou, J., Göttsche, F.-M., Wang, Z. W., Wu, H., Tang, W. B., et al. (2023). An atmospheric influence correction method for longwave radiation-based in-situ land surface temperature. *Remote Sensing of Environment*, *293*, 113611. https://doi.org/10.1016/j.rse.2023.113611

Pugachev, V. S. (2014). *Probability theory and mathematical statistics for engineers*. Elsevier.

Schaaf, C., & Wang, Z. (2015). MCD43A3 MODIS/Terra+Aqua BRDF/albedo daily L3 global - 500m V006 [Dataset]. NASA EOSDIS Land Processes DAAC. Retrieved from https://ladsweb.modaps.eosdis.nasa.gov/missions-and-measurements/products/MCD43A3

Wan, Z., Hook, S., & Hulley, G. (2015). MYD11A2 MODIS/Aqua land surface temperature/emissivity 8-Day L3 Global 1km SIN Grid V006 [Dataset]. NASA EOSDIS Land Processes DAAC. Retrieved from https://lpdaac.usgs.gov/products/myd11a2v006/#:~:text=MYD11A2%20v006&text=The%20MYD11A2%20Version%206%20product,average%20of%20all%20the%20corresponding

Ye, X. M., Xiao, X. B., Shi, J. B., & Ling, M. (2016). The new concepts of measurement error theory. *Measurement*, *83*, 96–105. https://doi.org/10.1016/j.measurement.2016.01.038